

The Gravitational Potential Near the Sun From SEGUE K-dwarf Kinematics

LAN ZHANG^{1,2,3}, HANS-WALTER RIX³, GLENN VAN DE VEN³, JO BOVY^{4,5},
CHAO LIU¹, and GANG ZHAO¹

Received _____; accepted _____

¹Key Lab of Optical Astronomy, National Astronomical Observatories, CAS, 20A Datun Road, Chaoyang District, 100012 Beijing, China

²Graduate University of the Chinese Academy of Sciences, 19A Yuquan Road, Shijingshan District, 100049 Beijing, China

³Max-Planck-Institute for Astronomy, Königstuhl 17, D-69117 Heidelberg, Germany

⁴Institute for Advanced Study, Einstein Drive, Princeton, NJ 08540, USA

⁵Hubble fellow

ABSTRACT

To constrain the Galactic gravitational potential near the Sun (~ 1.5 kpc), we derive and model the spatial and velocity distribution for a sample of 9000 K-dwarfs that have spectra from SDSS/SEGUE, which yield radial velocities and abundances ($[\text{Fe}/\text{H}]$ & $[\alpha/\text{Fe}]$). We first derive the spatial density distribution for stars of three abundance-selected sub-populations by accounting for the survey’s selection function. The vertical profile of these sub-populations are simple exponentials and their vertical dispersion profile is nearly isothermal. To model these data, we apply the ‘vertical’ Jeans Equation, which relates the observable tracer number density and vertical velocity dispersion to the gravitational potential or vertical force. We explore a number of functional forms for the vertical force law, and fit the dispersion and density profiles of all abundance selected sub-populations simultaneously in the same potential, and explore all parameter co-variances using MCMC. Our fits constrain a disk *mass* scale height $\lesssim 300$ pc and the total surface mass density to be $67 \pm 6 M_{\odot} \text{pc}^{-2}$ at $|z| = 1.0$ kpc of which the contribution from all stars is $42 \pm 5 M_{\odot} \text{pc}^{-2}$ (presuming a contribution from cold gas of $13 M_{\odot} \text{pc}^{-2}$). We find significant constraints on the local dark matter density of $0.0065 \pm 0.0023 M_{\odot} \text{pc}^{-3}$ ($0.25 \pm 0.09 \text{ GeV cm}^{-3}$). Together with recent experiments this firms up the best estimate of $0.0075 \pm 0.0021 M_{\odot} \text{pc}^{-3}$ ($0.28 \pm 0.08 \text{ GeV cm}^{-3}$), consistent with global fits of approximately round dark matter halos to kinematic data in the outskirts of the Galaxy.

Subject headings:

1. Introduction

Since the works of Oort (1932, 1960), determining the Galactic gravitational potential from the distribution and kinematics of stars has been one of the most instructive problem in Galactic disk study. Comparing it with the mass density distribution of visible material (stars and gas), one can derive the distribution of dark matter in the Galactic disk. Comparisons of such local dark matter estimations with rotation curve (Weber & de Boer 2010) constrain the shape of the dark matter distribution.

Kuijken & Gilmore (1989a,b,c, hereafter KG89a,b,c) pioneered a practical approach to constrain the Galactic potential near the Sun. They used K-dwarfs to estimate the surface mass density of the total gravitating mass and the mass density of dark matter by solving the ‘vertical’ Jeans’ Equation (i.e. in the 1D equation in the \hat{z} -direction), which correlates the space density and velocity of tracer stars. They found the identified (i.e. stellar and gaseous) surface density and the total surface mass density of all gravitating matter within $|z| \leq 1.1$ kpc from the Galactic plane near the Sun to be $48 \pm 8 M_{\odot} \text{pc}^{-2}$ and $71 \pm 6 M_{\odot} \text{pc}^{-2}$, respectively (KG89a,b,c Kuijken & Gilmore 1991, hereafter KG91). The uncertainties are mainly caused by the measured errors in distance and velocities of the K-dwarfs and the technique of recovering the vertical force K_z .

After KG91 there have been various other determinations of the disc surface mass density based on different stellar tracer: Flynn & Fuchs (1994, hereafter FF94) derived a surface mass density of $52 \pm 13 M_{\odot} \text{pc}^{-2}$ for the known disc matter. With Hipparcos data, Korchagin et al. (2003) focused $\Sigma_{|z| < 350 \text{ pc}} = 42 \pm 6 M_{\odot} \text{pc}^{-2}$, by using red giants; Holmberg & Flynn (2004, hereafter HF04) and Bienaymé et al. (2006) used K giants and red clump stars to estimate the disk surface density again, and the values are $\Sigma_{|z| < 1.1 \text{ kpc}} = 74 \pm 6 M_{\odot} \text{pc}^{-2}$ and $\Sigma_{|z| < 1.1 \text{ kpc}} \sim 57 - 79 \pm 6 M_{\odot} \text{pc}^{-2}$, respectively. The rather broad range in values implies that better data and techniques are needed to improve

the measurement of the density distribution of Galactic disk.

In this paper, using the large sample of K-dwarfs observed in SDSS/SEGUE (Yanny et al. 2009), we re-determine the disc surface mass density and mass density of dark matter. In a number of aspects, this work follows KG89b, in particular in constraining the “vertical force” K_z . However, the paper presents a number of new elements over previous studies in addition to the new large data set. We split the data into abundance selected sub-samples, which provide distinct probes of the same potential; and we simultaneously fit densities and kinematics using Markov-Chain Monte Carlo (hereafter MCMC) approach. Besides, we explore how the results depend on the functional forms for K_z .

This paper is organized as follows. In § 2, we describe the SEGUE/SDSS data, in particular we emphasize the spatial selection function, the distance determination, and the sub-samples of similar $[\text{Fe}/\text{H}]$ and $[\alpha/\text{Fe}]$. In § 3 we lay out how we determine the tracer number density and vertical velocity dispersion, and practicalities of solving the Jeans equation. The fitting results are shown and discussed in § 4 and § 5, with a summary in § 6.

2. DATA

For our analysis we aim for a sample of kinematics tracers that can be found in disk populations of various ages and metallicities, and which cover distance of 0.2 kpc to 2 kpc from the Sun. In the Sloan Digital Sky Survey (SDSS; York et al. 2000), K-dwarfs best satisfy these criteria. The Sloan Extension for Galactic Understanding and Exploration (SEGUE) is a subsurvey of SDSS-II (Abazajian et al. 2009) which operated from 2005 August to 2008 July, to probe the formation and evolution of our Galaxy. It obtained *ugriz* imaging of some 3500 deg² of sky outside of the SDSS-I footprint (Fukugita et al. 1996; Gunn et al. 1998, 2006; York et al. 2000; Smith et al.

2002; Stoughton et al. 2002; Abazajian et al. 2003, 2004, 2005, 2009; Pier et al. 2003; Ivezić et al. 2004; Adelman-McCarthy et al. 2006, 2007, 2008; Tucker et al. 2006), with special attention being given to scans of lower Galactic latitudes ($|b| < 35^\circ$) in order to better probe the disk/halo interface of the Milky Way. Overall, SEGUE obtained some 240,000 medium-resolution ($R \sim 2000$) spectra of stars in the Galaxy, selected to explore the nature of stellar populations from 0.3 kpc to 100 kpc (Yanny et al. 2009). The seventh data release (DR 7) is the final public data release from SDSS-II occurring in October 2008. SDSS-III, which is presently underway, has already completed the sub-survey SEGUE-II, an extension intended to obtain an additional sample of over 120,000 spectra for distant stars that are likely to be members of the outer-halo population of the Galaxy. Data from SEGUE-II have been distributed as part of the eighth public data release (DR 8) (Aihara et al. 2011a). The SEGUE Stellar Parameter Pipeline processes the wavelength- and flux-calibrated spectra generated by the standard SDSS spectroscopic reduction pipeline (Stoughton et al. 2002), obtains equivalent widths and/or line indices for more than 80 atomic or molecular absorption lines, and estimates T_{eff} , $\log g$, and $[\text{Fe}/\text{H}]$ through the application of a number of approaches (see Lee et al. 2008a,b; Allende Prieto et al. 2008; Smolinski et al. 2011).

2.1. K-dwarf selection

KG89b suggested that the tracer star in the present context should have the following properties: 1) they are phase-mixed and in dynamical equilibrium in Galactic potential; 2) they are common and distributed through all Galactic disc components; 3) the distance of tracer star can be well determined. Therefore, considering present SDSS/SEGUE observations, K-dwarfs are ideal stars which are used as tracer to measure the total disc mass. Compare to the SEGUE G-dwarfs (e.g. Bovy et al. 2012a), they have the advantage

that their minimal distance to be included in SDSS/SEGUE is almost two times closer.

Yanny et al. (2009) list the following color and magnitude cuts for identification and targeting of K-dwarf candidates:

$$14.5 \leq m_r \leq 19.0,$$

$$0.55 \leq (g - r) \leq 0.75.$$

In order to get reliable estimates for the ‘vertical’ (z) component of each star’s velocity, we added two more criteria, the existence of a good proper motion measurement and the existence of spectra in the data base

$$\text{error of proper motion} > 0.,$$

$$S/N > 15.$$

These criteria return 10,925 candidates in DR 8. However, DR 8 does not list $[\alpha/\text{Fe}]$, which is very important in subsequent analysis for K-dwarf candidates. Besides, proper motions of DR8 above declination $\delta > 41^\circ$ are worse than those of DR7 because of the astrometric calibration in DR8 (Aihara et al. 2011b). Thus, we use the $[\alpha/\text{Fe}]$ and proper motions from DR 7 for all of these candidates. To eliminate K-giants, only stars whose $\log g > 4.0$ are taken in the present work, which in the end leaves 9,157 stars. Fig. 1 shows the number density distribution of sample stars in $[\alpha/\text{Fe}]$ vs. $[\text{Fe}/\text{H}]$ space.

2.2. Abundance-selected sub-samples

As shown in Fig. 1, the distribution of the K-dwarf sample in the $[\alpha/\text{Fe}] - [\text{Fe}/\text{H}]$ plane is bi-modal, i.e. a metal-rich, α -deficient population and a metal-poor, α -enhanced one, as found by Lee et al. (2011) and Bovy et al. (2012a) for SDSS G-dwarfs.

Liu & van de Ven (2012) and Bovy et al. (2012b) have shown that the kinematics of ‘mono’-abundance sub-populations are relatively simple. Therefore, we will split our sample of K-dwarfs into subsets that are abundance-selected in the $[\alpha/\text{Fe}] - [\text{Fe}/\text{H}]$ plane (see Fig. 1, black boxes)

- metal-rich: $[\text{Fe}/\text{H}] \in [-0.5, 0.3]$, $[\alpha/\text{Fe}] \in [0., 0.15]$
- intermediate metallicity: $[\text{Fe}/\text{H}] \in [-1.0, -0.3]$, $[\alpha/\text{Fe}] \in [0.15, 0.25]$
- metal-poor: $[\text{Fe}/\text{H}] \in [-1.5, -0.5]$, $[\alpha/\text{Fe}] \in [0.25, 0.50]$

These sub-samples contain 3672, 1416, and 2001 stars, respectively. Of course, all these sub-population stars move in the same gravitational potential. We will present the analysis, separating the three sub-populations.

3. The Galactic potential near the Sun

For the present context, we only consider the simple problem of solving the Jeans equation for a one-dimensional slab and then to determine gravitational potential and hence density of matter near the Sun ($|R - R_\odot| = 1.0$ kpc and $|z| \lesssim 1.5$ kpc). Following KG89b, we assume that: the Galactic potential is the sum of contributions by observable matter and by dark matter and we assume the effective dark matter density is a constant. Hence, the ‘vertical’ Jeans equation can be written as (Binney & Tremaine 2008)

$$\frac{d}{dz} [\nu_\star(z)\sigma_z(z)^2] = -\nu_\star(z)\frac{d\Phi(z, R_\odot)}{dz} \quad (1)$$

where $\Phi(z, R_\odot)$ is the vertical gravitational potential in the Sun’s vicinity, i.e., we solve this equation for $R = \text{constant}$. Here, $\nu_\star(z)$ is the vertical number density of the tracer stellar population, and $\sigma_z(z)$ the vertical velocity dispersion of exactly those tracers.

The first derivative of $\Phi(z, R_\odot)$ is the gravitational force perpendicular to the galactic plane $K_z(z)$

$$K_z(z, R_\odot) \equiv -\frac{d\Phi(z, R_\odot)}{dz} \quad (2)$$

The (1D) Poisson equation relates the potential to the disk vertical mass density,

$$4\pi G\rho_{\text{tot}}(z, R_\odot) = \frac{d^2\Phi(z, R_\odot)}{dz^2} \quad (3)$$

where $\rho_{\text{tot}}(z, R_\odot)$ is the total mass density of all luminous components and the dark matter contribution.

Combining Eq. 1, Eq. 2, and Eq. 3, one obtains

$$\frac{d}{dz} [\nu_\star(z)\sigma_z(z)^2] = -\nu_\star(z)K_z(z, R_\odot) \quad (4)$$

$$4\pi G\rho_{\text{tot}}(z, R_\odot) = -\frac{d}{dz}K_z(z, R_\odot) \quad (5)$$

To solve Eq. 4 for a given tracer sub-population and derive the local mass density distribution by using Eq. 5, we proceed as follows:

- i) We determine $\nu_\star(z)$ and $\sigma_z(z)$ for each of the three tracer populations directly from the observations.
- ii) We presume the $\nu_\star(z)$ is a simple exponential (Bovy et al. 2012a) of unknown scale height \vec{h}_z . Here $\vec{h}_z = [h_{z,1}, h_{z,2}, h_{z,3}]$ correspond to the metal-rich, inter-intermediate metallicity, and metal-poor sub-samples, respectively.
- iii) We adopt a parameterized form of $K_z(z, R_\odot | \vec{p})$.
- iv) For each $[\vec{p}, \vec{h}_z]$, we fit for the best $\nu_\star(z)$ and $\sigma_z(z)$, and get the probability of the data given the parameters, i.e., $\mathcal{P}(\sigma_z, \nu_\star | \vec{p}, \vec{h})$
- v) We use a MCMC technique to sample the likelihood of the parameters and find the best $[\vec{p}, \vec{h}_z]$.

During the whole calculation, we assume a parameterized K_z model instead of gravitational model, because it makes the calculation easier. After getting a reasonable K_z form, gravitational potential can be derived by integration of K_z and mass density can be determined through the first derivative of K_z . Here we will describe the details step by step.

3.1. Tracer number density

3.1.1. Distance estimates and coordinate system

To obtain z and v_z of our sample stars in the Solar vicinity, we need to estimate their distance first. Given the color indices ($g - r$ and $g - i$), the r -band magnitude, and metallicity, the absolute magnitude is estimated by fitting to fiducial color-magnitude relations, calibrated through star cluster spectroscopy. The fiducial sequences for ($g - r, r$) and ($g - i, r$), based on YREC+MARCS isochrones, as described in An et al. (2009), are adopted. Then it is straightforward to determine the distance $D = 10^{\frac{r-M_r}{5}+1}$ pc.

Such distances were estimated by fitting the fiducials for the two colors above separately, yielding an average difference and standard deviation among these two distance estimates of 0.006 ± 0.077 . We use the average distance and the standard deviation from color-magnitude (hereafter CM) diagrams of ($g - r, r$) and ($g - i, r$) as the mean distance and its error, respectively.

With D estimated as above and observed Galactic longitude and latitude (l, b), we get the stars' position in Galactic cylindrical coordinates. We adopt a Galactocentric cylindrical

coordinate system in which $\hat{\mathbf{z}}$ -axis towards the North Galactic Pole ($b \simeq 90^\circ$), that is,

$$\begin{aligned} R &= \sqrt{D^2 \cos^2(b) - 2DR_\odot \cos(b) \cos(l) + R_\odot^2} \\ \theta &= \arctan \left[\frac{D \cos(b) \cos(l) - R_\odot}{D \cos(b) \sin(l)} \right] \\ Z &= D \sin(b) \end{aligned} \tag{6}$$

where $R_\odot = 8.0$ kpc is the adopted distance to the Galactic center (Reid 1993). In the following works, only the sample stars in the range $0.3 \text{ kpc} < |z| < 1.2 \text{ kpc}$ are used. This z -range is limited by the bright limit of SDSS data at the low end and by the legitimacy of treating the problem as 1-D ($\hat{\mathbf{z}}$ -direction) for large $|z|$.

3.1.2. Selection function

Any dynamical analysis need accurate knowledge of the spatial distribution of the kinematic tracer. Therefore, we need not only a well-defined spectroscopic sample of K-dwarfs with known fluxes and distances (or heights above the mid-plane) estimates, we also need to understand their selection function (Bovy et al. 2012c), which is what we lay out there.

In this coordinate system, each sub-sample can be divided in eight bins according to R and $\Delta R = R_{m+1} - R_m = 500$ pc. In each ΔR range, R is considered as a constant, and each sub-sample is also divided in 12 bins in $\hat{\mathbf{z}}$ direction. The width of the z bin, $\Delta z \equiv z_{i+1} - z_i$, is $\Delta z = 100$ pc. Here m and i are indices of R and z bins, respectively. In each z - R box

$$\nu_\star^{\text{sub}}(R_m, z_i) = \frac{N^{\text{sub}}(R_m, z_i)}{V_{\text{eff}}^{\text{sub}}(R_m, z_i)} \tag{7}$$

where $N^{\text{sub}}(R_m, z_i)$ and $V_{\text{eff}}^{\text{sub}}(R_m, z_i)$ are respectively the star number and the effective volume in a (z_i, R_m) box of a certain sub-sample. Because every targeted star of a given $(r, g - r)$ has a possibility to be in one particular sub-sample, each line of sight is a part of

the *search* volume for every abundance sub-sample. In our effective volume calculation, all lines-of-sights of all K-dwarfs are included, i.e.

$$V_{\text{eff}}^{\text{sub}}(R_m, z_i) = \sum_{q=1}^{n_{\text{sub}}} V_{\text{eff},q} \quad (8)$$

where n_{sub} is the total number of lines-of-sights of a given sub-sample and $V_{\text{eff},q}$ is the *search* volume of each line-of-sight.

It is in the calculation of the effective volume that the selection function enters explicitly. Some aspects of the SEGUE selection function are obvious. The apparent magnitude range brackets the possible distances of K-dwarfs, and the most nearby stars will be preferentially the brightest and coldest stars. At a given m_r and $g - r$, the effective survey volume is smaller for lower metallicity (hence less luminous) stars. Moreover, the SDSS targeting strategy implies that stars at lower latitude have a smaller probability of ending up in the spectroscopic sample, since a fixed number of targets is observed along each line of sight. In general, we need to derive the selection function, which gives the probability that a star of given M_r , $g - r$, $[\text{Fe}/\text{H}]$ ends up in the samples, as a function of D and (l, b)

Each SEGUE pointing which corresponds to an angular on-the-sky radius of 1.49° is observed with two plates, a SEGUE bright plate that targets stars with $14.0 < m_r < 17.8$ and faint plate that targets stars with $17.8 < m_r < 20.1$ (Yanny et al. 2009). In each plate, the distribution of spectroscopic sample in a CM box that satisfies the selection criteria is $n_{\text{spec}}(r, g - r)$, while the distribution of all photometric stars within the same plate that satisfy the same CM cuts is $n_{\text{photo}}(r, g - r)$. Integration of these distribution over all CM cuts results in N_{spec} and N_{photo} , leading to a plate weight

$$W_{\text{plate},j} \equiv \frac{N_{\text{spec},j}}{N_{\text{photo},j}} \quad (9)$$

where j is the index of plate. This plate weight should be a part of selection function.

Fig. 2 presents the cumulative distributions of spectroscopic and photometric samples in

the same selection criteria. It is clear that the selection weight for faint plates has an apparent magnitude dependence because of the dependence on signal-to-noise ratio of the probability of obtaining a good spectrum but no strong color dependence. Therefore, we make an approximation for this selection function, that is, it is a function of m_r .

This function is defined for all distance moduli, which is one for distance moduli that correspond to apparent magnitude insides of plates' magnitude range and zero for other situation. We combine the selection function in to the calculation of $V_{\text{eff},q}$, that is, the average metallicity of one particular sub-sample $\langle[\text{Fe}/\text{H}]\rangle$ is adopted to estimate the possible absolute magnitude, M_q , distance, D_q , and height above mid-plane, z_q , of a given $(r, g - r)$. Then

$$V_{\text{eff},q} = \frac{\pi}{3} \cdot W_{\text{plate},q} \cdot W_q \cdot \frac{\sin(\theta)}{\sin(b_q)} \cdot \frac{1}{2} [\cot(b_q - \theta) - \cot(b_q + \theta)] \cdot (z_{\text{upper}}^3 - z_{\text{lower}}^3) \quad (10)$$

where $\theta = 1.49^\circ$ is the diameter of SEGUE (and SDSS) spectroscopic plate (Yanny et al. 2009). Besides,

$$W_q = \begin{cases} 1, & \text{for } z_i \leq z_q \leq z_{i+1} \\ 0, & \text{otherwise} \end{cases} \quad (11)$$

$$z_{\text{upper}} = \text{Min}(z_{i+1}, D_{r,\text{max}} * \sin(b_q)) \quad (12)$$

$$z_{\text{lower}} = \text{Max}(z_i, D_{r,\text{min}} * \sin(b_q)) \quad (13)$$

$$D_{r,\text{min}} = 10^{\frac{r_{\text{min}} - M_q}{5} + 1} \text{ pc} \quad (14)$$

$$D_{r,\text{max}} = 10^{\frac{r_{\text{max}} - M_q}{5} + 1} \text{ pc} \quad (15)$$

where r_{min} and r_{max} are the magnitude limits of each plate. For SEGUE bright plate, $r_{\text{min}} = 14.0$ and $r_{\text{max}} = 17.8$, and for SEGUE faint plate, $r_{\text{min}} = 17.8$ and $r_{\text{max}} = 20.1$ (Yanny et al. 2009). In each z_i bin, the error bar of the tracer number density arises from the star count Poisson variance and it is estimated by means of Monte Carlo bootstrap ping (§ 15.6 of Press et al. 2007).

Fig. 3 presents the resulting (R, z) map of the tracer number density for each sub-population. From top to bottom, those plots correspond metal-rich, intermediate metallicity, and metal-poor sub-sample; from left to right, plots represent effective star number, effective volume, and natural logarithm of number density in each z - R box. In this figure, one can see that the scale-height of metal-rich sub-sample is shorter, but the scale-length of the same sub-population is longer. This result is similar as the studies of Galactic structure of Bovy et al. (2012c). If this number density result is projected onto \hat{z} direction, we get the vertical profile of the tracer number density.

3.2. Vertical velocity dispersions

To estimate $\sigma_z(z, [\text{Fe}/\text{H}], [\alpha/\text{H}])$, one could simply calculate the standard deviation of the observed $v_{z,i}$ values for each z bin of each sub-population. However, this would encompass the contribution arising from the measurement errors. Therefore, we use maximum likelihood technique described in van de Ven et al. (2006, Appendix A) to estimate the intrinsic velocity dispersion, corrected for all individual velocity errors.

In each z bin, the intrinsic velocity distribution of the stars is assumed as $\mathcal{L}(v_z)$. Each stellar velocity $v_{z,i}$ in this bin is the product of $\mathcal{L}(v_z)$ convolved with a delta function which is broadened by the observed uncertainties $\delta v_{z,i}$. For all N stars in the bin, the likelihood can be defined by

$$\mathcal{L}(\bar{v}_z, \sigma_z, \dots) = \prod_i^N \int_{-\infty}^{+\infty} \mathcal{L}(v) \frac{e^{-\frac{1}{2} \left(\frac{v_{z,i} - v_z}{\delta v_{z,i}} \right)^2}}{\sqrt{2\pi} \sigma_i} dv_z \quad (16)$$

where \mathcal{L} is a function of mean velocity \bar{v}_z , velocity dispersion σ_z and possible higher-order velocity moments. The velocity distribution $\mathcal{L}(v_z)$ can be recovered by maximizing the likelihood \mathcal{L} . To describe the velocity distribution, we use a parameterized Gauss-Hermite (GH) series (van der Marel & Franx 1993; Gerhard 1993) because it has the advantage that

it only requires the storage of the velocity moments ($\bar{v}_z, \sigma_z, h_{3,z}, h_{4,z}, \dots$) instead of the full velocity distribution and the convolution of Eq. 16 can be carried out analytically. This makes it feasible to apply the method to a large number of discrete measurements and to estimate the uncertainties on the extracted velocity moments by means of the Monte Carlo bootstrap method (§ 15.6 of Press et al. 2007).

Fig. 4 shows an example of a vertical velocity dispersion fit in $600 \text{ pc} < |z| < 700 \text{ pc}$ for the three sub-populations. This figure shows comparisons of different fitting methods. Red solid curves are the results of Gaussian fits without considering observed errors. Green and blue curves represent three and four moments GH fits using the method described above. For all $|z|$ bins of all sub-populations, the vertical velocity dispersion is overestimated by 2 - 4 km/s without considering observed errors.

For the metal-rich, intermediate metallicity, and metal-poor sub-samples, the measured $\sigma_{z,\text{obs}}(z)$ are in the ranges 17 - 26 km/s, 25 - 37 km/s, and 35 - 42 km/s, showing a increase with $|z|$. The $\sigma_{z,\text{obs}}(z)$ of different sub-populations are slightly increasing with the increasing of $|z|$. Moreover, $\sigma_{z,\text{obs}}(z)$ also increases with the decline of metallicity and the increasing of $[\alpha/\text{Fe}]$ (see Fig. 6, filled circles). We compare our observed $\sigma_{z,\text{obs}}(z)$ with recent study of Liu & van de Ven (2012), in which they adopted SEGUE G-dwarf of the Solar neighborhood. They used the splits at $[\alpha/\text{Fe}]=0.25$ and $[\text{Fe}/\text{H}]=-0.6$ to divide their sample into three groups: group I of α -young metal-rich stars which correspond to our metal-rich and intermediate metallicity sub-samples, group II of α -old metal-rich stars, and group III of α -old metal-poor stars which correspond to our metal-poor sub-sample (Fig. 3, Liu & van de Ven 2012). For the three groups, they found that the $\sigma_{z,\text{obs}}(z)$ is about 20 - 40 km/s, 35 - 50 km/s, and 40 - 55 km/s, respectively (Fig. 4, Liu & van de Ven 2012). These $\sigma_{z,\text{obs}}(z)$ are in good agreement with our measurements. Bovy et al. (2012c) also studied the vertical motions of mono-abundance sub-populations in the Galactic disk by

G-dwarf, and found that $\sigma_{z,\text{obs}}(z)$ varies from 15 – 25 km/s, 20 – 30 km/s, and 30 – 50 km/s for stars in our metal-rich, inter-intermediate metallicity, and metal-poor selection bins, respectively, which are consistent with our measurements.

3.3. Functional forms for K_z

Given the tracer number density and vertical velocity dispersion probes, we investigate different parameterized $K_z(z)$ forms to solve Eq. 1 and derive the corresponding expression for $\sigma_z(z)$. $K_z(z)$ is contributed both by the baryonic components and the dark matter. According to the discussion of KG89b, all $K_z(z)$ forms should satisfy the following assumption: (1) the halo and disk contributions are degenerate when $|z| \ll$ scale height; (2) disk contribution is approximate from a thin mass sheet when $|z| \gg$ scale height. We considered five different parameterized forms of $K_z(z)$, two of which we discuss below, while the other three are given in the Appendix,

i) **KG89 model**

$$K_z = 2\pi G \left[\Sigma_\star \frac{z}{\sqrt{z^2 + z_h^2}} + \Sigma_{\text{gas}} \right] + 4\pi G \rho_{\text{DM}} z \quad (17)$$

ii) **Exponential model**

$$K_z = 2\pi G \left\{ \Sigma_\star \left[1 - \exp\left(-\frac{z}{z_h}\right) \right] + \Sigma_{\text{gas}} \right\} + 4\pi G \rho_{\text{DM}} z \quad (18)$$

Here Σ_\star is the surface mass density in stars, $\Sigma_{\text{gas}} = 13.2 M_\odot \text{pc}^{-2}$ is the surface mass density of gaseous components which is taken from the disc mass model of Flynn et al. (2006), and ρ_{DM} is the effective dark matter contribution, and z_h is the scale height of mass density.

In these models we use $\Sigma_\star + \Sigma_{\text{gas}}$ rather than ρ_{disk} , because ρ_{disk} and z_h are degenerate, i.e., one can not constrain ρ_{disk} and z_h separately at the same time.

For the exponential model, the corresponding vertical dispersion profile can be derived analytically:

$$\sigma_{z,\text{sub}}^2 = 2\pi G h_z^{\text{sub}} \left\{ \Sigma_{\star} \left[1 - \frac{z_h}{h_z^{\text{sub}} + z_h} \exp\left(-\frac{z}{z_h}\right) \right] + \Sigma_{\text{gas}} \right\} + 4\pi G \rho_{\text{DM}} h_z^{\text{sub}} (z + h_z^{\text{sub}}) \quad (19)$$

For the other K_z forms we infer $\sigma_{z,\text{sub}}$ through numerical integration.

3.4. Obtaining the PDFs for the model parameters

The predictions for $\sigma_{z,\text{sub}}(z)$ are based on 6 parameters for each $K_z(z, R_{\odot})$ model, which may have considerable covariance. At the same time, we have a parameterized model for the vertical tracer density profile, and we want to derive constraints on the gravitational force, marginalized over the scale height parameters. To explore the parameter space efficiently and to account for parameter degeneracies, we use a MCMC approach, which provides a straightforward and powerful way of estimating the probability distributions (PDF) for all the model parameters and their degree of uncertainty (§ 15.8 of Press et al. 2007).

The objective is to calculate the probability of the data given the parameters, where the ‘data’ are the tracer number density and the vertical velocity dispersion profiles described above. The probabilities for $\sigma_z(z)$ and $\nu_{\star}(z)$ in each $|z|$ bin are independent, therefore, the logarithm of the likelihood of the data given the parameters can be written as

$$\begin{aligned} \ln \mathcal{P} = & - \sum_j^N \ln(2\pi \epsilon_{\sigma_{z,\text{obs},j}} \epsilon_{\nu_{\text{obs},j}}) - \\ & \sum_j^N \frac{1}{2} \left(\frac{\sigma_{z,\text{fit},j} - \sigma_{z,\text{obs},j}}{\epsilon_{\sigma_{z,\text{obs},j}}} \right)^2 - \sum_j^N \frac{1}{2} \left(\frac{\nu_{\text{fit},j} - \nu_{\text{obs},j}}{\epsilon_{\nu_{\text{obs},j}}} \right)^2 \end{aligned} \quad (20)$$

where N is the total number of $|z|$ bin, \vec{p} are the parameters of gravitational model, and $\vec{h} = [h_{z,1}, h_{z,2}, h_{z,3}]$ are the scale heights of tracer number density of different sub-populations.

The trace number density profile is modeled by single exponential,

$$\nu_{\star,s}(z) = \nu_{0,s} \times \exp\left(-\frac{z}{h_{z,s}}\right) \quad (21)$$

where the subscript s denotes the different abundance-dependent sub-populations. In order to reduce the number of parameters by eliminating $\nu_{0,s}$ from Eq. 21, we calculate $\nu_{0,s}$ for each sub-population by

$$\frac{\partial \chi^2(\nu)}{\partial \nu_{0,s}} = 0, \quad (22)$$

yielding

$$\nu_{0,s} = \sum_j^N \frac{\exp(-z_j)}{\epsilon_{\nu_{\text{obs}},s,j}} \nu_{\text{obs},s,j} \bigg/ \sum_j^N \frac{\exp(-z_j)}{\epsilon_{\nu_{\text{obs}},s,j}} \exp\left(-\frac{z_j}{h_{z,s}}\right). \quad (23)$$

All other parameters are estimated by running a MCMC chain of typically 50,000 steps, after a burn-in. In the Markov chain, the parameters of the gravitational model and scale heights of tracer densities $[\vec{p}_n, \vec{h}_{z,n}]$ are chosen from a multivariate normal distribution of $[\vec{p}_{n-1}, \vec{h}_{n-1}]$, with the covariance of $[\vec{p}, \vec{h}_z]$ chosen to yield a total acceptance rate in the MCMC Chain of about 20% \sim 30%. We use the results of all steps to represent $[\vec{p}, \vec{h}_z]$ and their distributions, by counting the rejected steps as repeat ones. After sampling the PDF for parameters for each K_z model, χ_{tot}^2 between the observed values ($\sigma_{z,\text{obs}}$ and $\nu_{\star,\text{obs}}$) and model predicted ones ($\sigma_{z,\text{mod}}$ and $\nu_{\star,\text{mod}}$) is calculated to explore how the models form the different K_z families compare:

$$\begin{aligned} \chi_{\text{tot}}^2 &= \chi_{\sigma_z}^2 + \chi_{\nu_{\star}}^2 \\ &= \sum_{s=1}^3 \left[\sum_j^N \left(\frac{\sigma_{z,j,s,\text{mod}} - \sigma_{z,j,s,\text{obs}}}{\epsilon_{\sigma_{z,j,s,\text{obs}}}} \right)^2 + \sum_j^N \left(\frac{\nu_{j,s,\text{mod}} - \nu_{j,s,\text{obs}}}{\epsilon_{\nu_{j,s,\text{obs}}}} \right)^2 \right], \end{aligned} \quad (24)$$

where s is the indices of sub-sample, j is the number of $|z|$ bins.

4. Results

The above procedure results in PDFs for the K_z and ν_* parameters, which are presented in Figs. 5 – 10. The best fitting results and recovered parameters for all K_z gravitational force law models are listed in Table 1.

4.1. Vertical tracer density profiles

Fig. 5 shows the fits to the vertical tracer density profiles. Filled circles are values derived directly from observations, which are the average value of R columns ($7 \text{ kpc} \leq R \leq 9 \text{ kpc}$) of the right panel of Fig. 3. Dashed lines are the predictions for $\nu_{*,s}(z)$ (Eq. 21) for two different K_z models, and the shaded regions represent the samplings of the last 200 steps in the MCMC chain. Red, green, and blue symbols represent metal-rich, intermediate metallicity, and metal-poor sub-population, respectively. Each sub-population has a simple and single exponential structure, and the scale height is increasing with the decline of metallicity (as seen in Liu & van de Ven 2012; Bovy et al. 2012c).

The joint parameter PDFs show that the tracer scale height, \vec{h}_z is independent of the K_z model parameters (see Fig. 9). The scale-heights we find for different abundance-select tracer sub-populations are 230 - 260 pc, 450 - 510 pc, and 800 - 1000 pc (see Table 1), for all K_z families. The minor differences caused by different models are within the 68% central region of the h_z PDF.

These findings are in accord with recent results by Bovy et al. (2012c) and Liu & van de Ven (2012). In their work, they adopted G-dwarfs from SDSS/DR7 to analysis the relationship between the distribution of Galactic disc stars and their metallicity in each narrow $[\alpha/\text{Fe}]$ - $[\text{Fe}/\text{H}]$ box. They concluded that the scale-height increases continually from 200 pc to 1200 pc with the decline of metallicity.

4.2. Vertical dispersion profiles

As discussed in 3.2, the $\sigma_{z,\text{obs}}(z)$ shown in Figure 6, have already been corrected for the velocity errors of the individual stars within each $|z|$ bin. In these plots, we also summarize $\sigma_{z,\text{mod}}(z)$ predicted by different K_z models. The results reflect simultaneous fit to all three sub-populations. If the $\sigma_{z,\text{obs}}(z)$ is fitted for each sub-population separately, there is some slight tension between the fits to the individual sub-populations and the simultaneous fit. The difference of $\sigma_{z,\text{mod}}(z)$ given by different models is smaller than the error of observed $\sigma_{z,\text{obs}}(z)$, as in the case of the scale-height predictions of vertical number density. That is, for the three sub-population, $\sigma_{z,\text{mod}}(z)$ is in the range of 16 - 20 km/s, 25 - 29 km/s, and 35 - 43 km/s (see Table 1), respectively.

We note again, that previous studies of $K_z(z)$ by KG89a,b,c, HF04, Siebert et al. (2003), Garbari et al. (2012, hereafter G12) and Bovy & Tremaine (2012, hereafter BT12) had not, or could not, split their tracer samples a priori into abundance sub-bins with nearly isothermal $\sigma_z(z)$ profiles. In samples with a wide metallicity range $\sigma_z(z)$ will rise with $|z|$ simply because the mix of mono-abundance populations will change. To disentangle a rising $\sigma_z(|z|)$ due to a dark matter halo from the effect of population mixing, these studies had to model the metallicity distribution, which turned out to be an important source of systematic errors. Fitting simultaneously to populations that have been split *a priori* by their abundances, as done here, reduces this source of systematics.

4.3. The vertical gravitational force K_z

Fig. 7 shows $K_z(z)$ implied by our fits using the KG89b and exponential families for the ‘vertical force law’. The dashed fat lines show $K_z(z)$ for the most likely parameters, and the band of grey lines show a 1σ sampling of the PDF for $K_z(z)$. For both the KG89b

and the exponential families of $K_z(z)$ show a number of generic features in Fig. 7: they start out with a finite value for small $|z|$, as we have fixed a prior contribution from a thin layer of the cold gas with $\sim 13 M_\odot \text{pc}^{-2}$; then K_z rises steeply to $\sim 300 \text{ pc}$ (reflecting the mass scale height of the stellar disk) and then flattens out; beyond $\sim 500 \text{ pc}$ the slower rise in K_z reflects the dark matter halo term.

On the basis of $K_z(z)$, we can derive the total surface density at $|z| = 1.0 \text{ kpc}$. We get $\Sigma_{\text{tot},|z|<1.0 \text{ kpc}}^{\text{KG89}} = 67 \pm 6 M_\odot \text{pc}^{-2}$ for the KG89 model and $\Sigma_{\text{tot},|z|<1.0 \text{ kpc}}^{\text{Exp}} = 66 \pm 8 M_\odot \text{pc}^{-2}$ for the exponential model. It is clear that $\Sigma_{\text{tot},|z|<1.0 \text{ kpc}}$ is robustly constrained, irrespective of the K_z model. Our modelling also constrains the mass scale height, $245_{-245}^{+188} \text{ pc}$ for KG89 and 200_{-200}^{+100} for the exponential model (see Fig. 8). Within these uncertainties, this is consistent with the 180 pc from Hill et al. (1979) by analyzing A and F dwarfs and $390_{-120}^{+330} \text{ pc}$ of Siebert et al. (2003), found by using high resolution spectral data of red clump stars. Taken together this forms up the picture that there is a dominant mass layer near the disk mid-plane (presumably baryonic) that is rather flat.

For comparison with literature studies, we also explicitly estimate the total surface density of baryonic matter within $|z| < 1.1 \text{ kpc}$, $\Sigma_{\text{bar},|z|<1.1 \text{ kpc}} = \Sigma_\star + \Sigma_{\text{gas}}$, which we find to be $\Sigma_{\text{bar},|z|<1.1 \text{ kpc}}^{\text{KG89}} = 55 \pm 5 M_\odot \text{pc}^{-2}$, and $\Sigma_{\text{bar},|z|<1.1 \text{ kpc}}^{\text{Exp}} = 54 \pm 8 M_\odot \text{pc}^{-2}$, respectively. These values are slightly higher than $48 \pm 8 M_\odot \text{pc}^{-2}$ derived by KG89b, but are in perfect agreement with the value of $52 \pm 13 M_\odot \text{pc}^{-2}$ of FF94 and $53 \pm 6 M_\odot \text{pc}^{-2}$ of HF04.

The local mass densities of dark matter recovered by our models are $\rho_{\text{DM}}^{\text{KG89}} = 0.0065 \pm 0.0023 M_\odot \text{pc}^{-3}$ ($0.25 \pm 0.09 \text{ GeV cm}^{-3}$)¹ and $\rho_{\text{DM}}^{\text{Exp}} = 0.0060 \pm 0.0020 M_\odot \text{pc}^{-3}$ ($0.23 \pm 0.08 \text{ GeV cm}^{-3}$), marginalized over the other parameters.. We explored the parameter degeneracies by MCMC (see Fig. 10), which recover the known degeneracy

¹ $1 \text{ GeV cm}^{-3} \simeq 0.0263158 M_\odot \text{pc}^{-3}$

between surface mass density of stars and volume mass density of dark matter: lower Σ_* correlates with higher ρ_{DM} , at an approximately constant total surface mass density.

5. Discussion

We have presented an analysis of the vertical Galactic potential at the Solar radius, drawing on ~ 9000 K-dwarfs from SDSS/SEGUE. In many ways, the analysis followed the approach initially laid out by KG89 and implemented by several other groups in the mean-time (Siebert et al. 2003, HF04, G12, BT12). In comparison to most previous studies, our analysis has a number of new elements: we have a substantially larger sample than previous analyses; we have taken explicit account of the abundance-dependent spatial selection function of our sample for the analysis; we have simultaneously fit for several abundance-selected nearly-isothermal sub-populations that ‘feel’ the same gravitational potential, and we have matched the kinematics and the spatial distribution simultaneously; we have explored to which extent the choice of the functional form for K_z affects the results.

As laid out in the previous Section, we find good constraints on $\Sigma_{\text{tot},|z|<1.0 \text{ kpc}}$ and some constrains on thickness of the disk *mass* layer: $z_h: \Sigma_{\text{tot},|z|<1.0 \text{ kpc}} = 67 \pm 6 M_\odot \text{ pc}^{-2}$ and $z_h \lesssim 300 \text{ pc}$, irrespective of the functional form we assume for K_z . This is also among the first studies to find significant ($> 2\sigma$) constraints on the local dark matter density, $\rho_{\text{DM}} = 0.0065 \pm 0.0023 M_\odot \text{ pc}^{-3}$ ($0.25 \pm 0.09 \text{ GeV cm}^{-3}$). Fig. 10 shows the expected degeneracy between total surface density of visible matter and dark matter density: lower Σ_* corresponds to a higher ρ_{DM} for a given total surface density. However, these uncertainties do not include the systematic errors from misestimated photometric distances. For example, binary contamination would make the inferred distances smaller, and the distance estimation of An et al. (2009) which we adopted in the present work is also $\sim 9\%$ smaller than the one of Ivezić et al. (2008). We explore distance systematic in particular

for their implications on the dark matter density: if a 10% distance systematic error is considered, the inferred change of ρ_{DM} is only 10%.

Overall, our results are consistent with earlier studies, as Fig. 11 shows, which compares our inference about K_z and about the total surface density $\Sigma_{\text{tot}}(z)$ with previous studies. The value derived by KG91 is $\Sigma_{\text{tot},|z|<1.1 \text{ kpc}} = 71 \pm 6 M_{\odot} \text{ pc}^{-2}$ and $\rho_{\text{DM}} = 0.01 \pm 0.005 M_{\odot} \text{ pc}^{-3}$. In the calculation of HF04, $\Sigma_{\text{tot},|z|<1.1 \text{ kpc}} = 74 \pm 6 M_{\odot} \text{ pc}^{-2}$ and $\rho_{\text{DM}} = 0.007 M_{\odot} \text{ pc}^{-3}$, whereas the latter results are in a good agreement with ours.

However, G12 have re-analyzed the K dwarf sample from KG89b using the Jeans equation (Garbari et al. 2011) and they found a much large value of $\rho_{\text{DM}} = 0.025_{-0.013}^{+0.014} M_{\odot} \text{ pc}^{-2}$ ($0.85_{-0.49}^{+0.57} \text{ GeV cm}^{-3}$). G12 use similar data as we do in this paper, but the sample is approximately five times smaller and the data have neither $[\text{Fe}/\text{H}]$ nor $[\alpha/\text{Fe}]$ measured; the KG89b sample, however, has a simpler spatial selection function than the SEGUE K dwarf sample. There are a number of reasons why G12 may be overestimating the local dark-matter density: as they do not have measurements of $[\text{Fe}/\text{H}]$ for the stars in their sample, their photometric distances are less accurate and less precise, and the metallicity distribution that they adopt from SEGUE has not been corrected for selection effects. The corrected metallicity distribution has a vertical gradient close to the $-0.3 \text{ dex kpc}^{-1}$ gradient assumed by KG91 (Schlesinger et al. 2012); Appendix A of G12 shows that this leads to a slightly lower ρ_{DM} . G12 also use a strong prior for the structure of the baryonic disk through their use of 15 isothermal baryonic components with fixed velocity dispersions. This model requires “dark matter” to account for any imperfections in the disk model. Most importantly, G12 cannot separate sub-populations based on elemental abundances as we do here, such that they may potentially mistake population gradients in $\sigma_z(z)$ and $h_z(z)$ for the signature of dark matter.

On the other hand, our estimates are in very good agreement (Fig. 12) with the recent

determination of ρ_{DM} by BT12, who re-analyzed the data by Moni Bidin et al. (2012). They used the assumption of $\partial V_c / \partial R = 0$ to correct the model of Moni Bidin et al. (2012), and derived a dark matter density of $\rho_{\text{DM}} = 0.008 \pm 0.003 M_{\odot} \text{pc}^{-3}$ ($0.30 \pm 0.11 \text{ GeV cm}^{-3}$).

Fig. 12 puts the recent local ρ_{DM} estimate from K_z constraints into context. The histogram with the gray shading in its center represents the results from G12, the one with black is from BT12 and the one with red is from the present work (hereafter Z12). The BT12 histogram reflects their ρ_{DM} PDF including systematic errors; for Z12 several of these error sources have been addressed systematically, and the distance uncertainties have been incorporated as a systematic error term in the Z12 histogram in Fig. 12. Therefore, the results shown in Fig. 12 from Z12 and BT12 should be on comparable footing. The joint PDF emerging from these three recent experiments is shown as the thick black histogram in Fig 12, indicating $\rho_{\text{DM}} = 0.0075 \pm 0.0021 M_{\odot} \text{pc}^{-3}$ ($0.28 \pm 0.08 \text{ GeV cm}^{-3}$).

One can put these ‘local’ estimates of the dark matter density into the context of the expectations from the global fits of the Galactic dark matter halo: with a spherical NFW cold dark matter density profile (Navarro et al. 1996) and the parameters of Xue et al. (2008) (virial mass $M_{\text{vir}} = 0.91_{-0.18}^{+0.27} \times 10^{12} M_{\odot}$, virial radius $r_{\text{vir}} = 267_{-19}^{+24} \text{ kpc}$, and $c = 12.0$), one would expect that the dark matter density at R_{\odot} is $\rho_{\text{DM}}(R_{\odot}) = 0.0063 M_{\odot} \text{pc}^{-3}$, which is in very good, perhaps even fortuitous, agreement with our present work.

Taken together with the existing work, our results continue to point towards a picture that the local Galactic potential is dominated by a fairly thin layer of stars and gas plus a dark matter density that is in accord with global fits to Galactic halo.

It may seem surprising, why our limits we derive are not much tighter than those obtained by KG89b and subsequent work, based on smaller samples. This is in good part due to the fact that we used far fewer prior constraints on the models. E.g. we *fit* for the mass scale-height of the disk (z_h) rather than assume it; similarly, we fit for the scale

height of the tracers simultaneously with the kinematic fit; and we have explored a range of functional forms for K_z . Marginalizing over these factors, apparently leads to a seemingly similar error on the parameters than other more restricted analysis with smaller samples.

6. Conclusion

We have analyzed the K-dwarfs from SDSS/SEGUE for determining the total surface mass density and dark matter density in the local Galactic disc. At first, we divide our sample into three sub-populations through their $[\text{Fe}/\text{H}]$ and $[\alpha/\text{Fe}]$. After considering the spatial selection function, the Galactic vertical number density profiles for different sub-populations are inferred from star counting. Secondly, we use maximum likelihood and Gauss-Hermite series to calculate the vertical velocity dispersion profile of each sub-population. Then different parameterized K_z forms are used to solve the ‘vertical’ Jeans equation. We fit the observed vertical number density and vertical velocity dispersion profiles of the three sub-populations simultaneously, using MCMC to recover the PDFs of the parameters of the ‘vertical force law’. In our results, for each sub-population, the vertical number density is approximately single exponential profile and the vertical velocity dispersion is nearly isothermal. The scale height of number density profile and the vertical velocity dispersion increase with the decline of metallicity. Presuming that there is a thin gas layer with $\Sigma_{\text{gas}} = 13 M_{\odot} \text{pc}^{-2}$, we derive a total surface mass density of $67 \pm 6 M_{\odot} \text{pc}^{-2}$ at 1.0 kpc from the mid-plane, of which the contribution of all stars is $42 \pm 5 M_{\odot} \text{pc}^{-2}$ and we infer a local dark matter density of $\rho_{\text{DM}} = 0.0065 \pm 0.0023 M_{\odot}/\text{pc}^{-3}$ ($0.25 \pm 0.09 \text{ GeV cm}^{-3}$).

We would like to thank Constance Rockosi for the discussion of distance calculation. LZ acknowledges support of NSFC grant 10903012 and from the MPG-CAS student program.

HWR, GvdV, and JB acknowledge partial support from Sonderforschungsbereich SFB 881 “The Milky Way System” (subproject A3 and A7) funded by the German Research Foundation. JB was supported by NASA through Hubble Fellowship grant HST-HF-51285.01 from the Space Telescope Science Institute, which is operated by the Association of Universities for Research in Astronomy, Incorporated, under NASA contract NAS5-26555.

Funding for SDSS-III has been provided by the Alfred P. Sloan Foundation, the Participating Institutions, the National Science Foundation, and the U.S. Department of Energy Office of Science. The SDSS-III web site is <http://www.sdss3.org/>.

SDSS-III is managed by the Astrophysical Research Consortium for the Participating Institutions of the SDSS-III Collaboration including the University of Arizona, the Brazilian Participation Group, Brookhaven National Laboratory, University of Cambridge, Carnegie Mellon University, University of Florida, the French Participation Group, the German Participation Group, Harvard University, the Instituto de Astrofísica de Canarias, the Michigan State/Notre Dame/JINA Participation Group, Johns Hopkins University, Lawrence Berkeley National Laboratory, Max Planck Institute for Astrophysics, Max Planck Institute for Extraterrestrial Physics, New Mexico State University, New York University, Ohio State University, Pennsylvania State University, University of Portsmouth, Princeton University, the Spanish Participation Group, University of Tokyo, University of Utah, Vanderbilt University, University of Virginia, University of Washington, and Yale University.

A. Other Model Functional Forms for K_z

Besides the two models for K_z described in § 3.3, we also explore other three models to determine the total surface mass density and the mass density of dark matter, with the

purpose of checking whether the astrophysical inferences depend on the choice of these functional forms:

iii) **Error function model**

$$K_z = 2 \pi G \left[\Sigma_\star \operatorname{erf} \left(\frac{z}{z_h} \right) + \Sigma_{\text{gas}} \right] + 4 \pi G \rho_{\text{DM}} z \quad (\text{A1})$$

iv) **General model I** This form is an extension of KG model. We assume K_z as the form of

$$K_z = 2 \pi G \left[\Sigma_\star \left(\frac{z^\beta}{z^\gamma + z_h^\beta} \right)^{\frac{1}{\beta}} + \Sigma_{\text{gas}} \right] + 4 \pi G \rho_{\text{DM}} z \quad (\text{A2})$$

v) **General Model II** To reduce the number of free parameters, we set $\beta = \gamma$ and get

$$K_z = 2 \pi G \left[\Sigma_\star \left(\frac{z^\beta}{z^\beta + z_h^\beta} \right)^{\frac{1}{\beta}} + \Sigma_{\text{gas}} \right] + 4 \pi G \rho_{\text{DM}} z \quad (\text{A3})$$

We followed the same parameter estimation approach for these models and calculated the total χ^2 between observed $\sigma_{z,\text{obs}}$ and ν_\star and the model predictions. The error function model and the general model II yield similar results for the surface density of visible matter and dark matter density as the KG89 and exponential models discussed in the main text. Only the general models I, where the exponents γ and β are independent yields to a degree of parameter degeneracy that makes the resulting $K_z(z)$ difficult to interpret. But overall this confirms that among physically plausible families of K_z , the particular choice matters little.

REFERENCES

- Abazajian, K., Adelman-McCarthy, J. K., Agüeros, M. A., et al. 2004, *AJ*, 128, 502
- Abazajian, K., Adelman-McCarthy, J. K., Agüeros, M. A., et al. 2005, *AJ*, 129, 1755
- Abazajian, K., Adelman-McCarthy, J. K., Agüeros, M. A., et al. 2003, *AJ*, 126, 2081
- Abazajian, K. N., Adelman-McCarthy, J. K., Agüeros, M. A., et al. 2009, *ApJS*, 182, 543
- Adelman-McCarthy, J. K., Agüeros, M. A., Allam, S. S., et al. 2008, *ApJS*, 175, 297
- Adelman-McCarthy, J. K., Agüeros, M. A., Allam, S. S., et al. 2007, *ApJS*, 172, 634
- Adelman-McCarthy, J. K., Agüeros, M. A., Allam, S. S., et al. 2006, *ApJS*, 162, 38
- Aihara, H., Allende Prieto, C., An, D., et al. 2011a, *ApJS*, 193, 29
- Aihara, H., Allende Prieto, C., An, D., et al. 2011b, *ApJS*, 195, 26
- Allende Prieto, C., Sivarani, T., Beers, T. C., et al. 2008, *AJ*, 136, 2070
- An, D., Pinsonneault, M. H., Masseron, T., et al. 2009, *ApJ*, 700, 523
- Bienaymé, O., Soubiran, C., Mishenina, T. V., Kovtyukh, V. V., & Siebert, A. 2006, *A&A*, 446, 933
- Binney, J. & Tremaine, S. 2008, *Galactic Dynamics: Second Edition*, ed. Binney, J. & Tremaine, S. (Princeton University Press)
- Bovy, J., Rix, H.-W., & Hogg, D. W. 2012a, *ApJ*, 751, 131
- Bovy, J., Rix, H.-W., Hogg, D. W., et al. 2012b, *ApJ*, 755
- Bovy, J., Rix, H.-W., Liu, C., et al. 2012c, *ApJ*, 753, 148

- Bovy, J. & Tremaine, S. 2012, *ApJ*, 756, 89
- Flynn, C. & Fuchs, B. 1994, *MNRAS*, 270, 471
- Flynn, C., Holmberg, J., Portinari, L., Fuchs, B., & Jahreiß, H. 2006, *MNRAS*, 372, 1149
- Fukugita, M., Ichikawa, T., Gunn, J. E., et al. 1996, *AJ*, 111, 1748
- Garbari, S., Liu, C., Read, J. I., & Lake, G. 2012, *ArXiv e-prints*
- Garbari, S., Read, J. I., & Lake, G. 2011, *MNRAS*, 416, 2318
- Gerhard, O. E. 1993, *MNRAS*, 265, 213
- Gunn, J. E., Carr, M., Rockosi, C., et al. 1998, *AJ*, 116, 3040
- Gunn, J. E., Siegmund, W. A., Mannery, E. J., et al. 2006, *AJ*, 131, 2332
- Hill, G., Hilditch, R. W., & Barnes, J. V. 1979, *MNRAS*, 186, 813
- Holmberg, J. & Flynn, C. 2004, *MNRAS*, 352, 440
- Ivezić, Ž., Lupton, R. H., Schlegel, D., et al. 2004, *Astronomische Nachrichten*, 325, 583
- Ivezić, Ž., Sesar, B., Jurić, M., et al. 2008, *ApJ*, 684, 287
- Korchagin, V. I., Girard, T. M., Borkova, T. V., Dinescu, D. I., & van Altena, W. F. 2003, *AJ*, 126, 2896
- Kuijken, K. & Gilmore, G. 1989a, *MNRAS*, 239, 605
- Kuijken, K. & Gilmore, G. 1989b, *MNRAS*, 239, 651
- Kuijken, K. & Gilmore, G. 1989c, *MNRAS*, 239, 571
- Kuijken, K. & Gilmore, G. 1991, *ApJ*, 367, L9

- Lee, Y. S., Beers, T. C., An, D., et al. 2011, *ApJ*, 738, 187
- Lee, Y. S., Beers, T. C., Sivarani, T., et al. 2008a, *AJ*, 136, 2022
- Lee, Y. S., Beers, T. C., Sivarani, T., et al. 2008b, *AJ*, 136, 2050
- Liu, C. & van de Ven, G. 2012, *MNRAS*, in press
- Moni Bidin, C., Carraro, G., Méndez, R. A., & Smith, R. 2012, *ApJ*, 751, 30
- Navarro, J. F., Frenk, C. S., & White, S. D. M. 1996, *ApJ*, 462, 563
- Oort, J. H. 1932, *Bull. Astron. Inst. Netherlands*, 6, 249
- Oort, J. H. 1960, *Bull. Astron. Inst. Netherlands*, 15, 45
- Pier, J. R., Munn, J. A., Hindsley, R. B., et al. 2003, *AJ*, 125, 1559
- Press, W. H., Teukolsky, S. A., Vetterling, W. T., & Flannery, B. P. 2007, *Numerical Recipes. The art of scientific computing*, ed. Press, W. H., Teukolsky, S. A., Vetterling, W. T., & Flannery, B. P.
- Reid, M. J. 1993, *ARA&A*, 31, 345
- Schlesinger, K. J., Johnson, J. A., Rockosi, C. M., et al. 2012, *ApJ*, submitted, arXiv:1112.2214
- Siebert, A., Bienaymé, O., & Soubiran, C. 2003, *A&A*, 399, 531
- Smith, J. A., Tucker, D. L., Kent, S., et al. 2002, *AJ*, 123, 2121
- Smolinski, J. P., Lee, Y. S., Beers, T. C., et al. 2011, *AJ*, 141, 89
- Stoughton, C., Lupton, R. H., Bernardi, M., et al. 2002, *AJ*, 123, 485

Tucker, D. L., Kent, S., Richmond, M. W., et al. 2006, *Astronomische Nachrichten*, 327, 821

van de Ven, G., van den Bosch, R. C. E., Verolme, E. K., & de Zeeuw, P. T. 2006, *A&A*, 445, 513

van der Marel, R. P. & Franx, M. 1993, *ApJ*, 407, 525

Weber, M. & de Boer, W. 2010, *A&A*, 509, A25

Xue, X. X., Rix, H. W., Zhao, G., et al. 2008, *ApJ*, 684, 1143

Yanny, B., Rockosi, C., Newberg, H. J., et al. 2009, *AJ*, 137, 4377

York, D. G., Adelman, J., Anderson, Jr., J. E., et al. 2000, *AJ*, 120, 1579

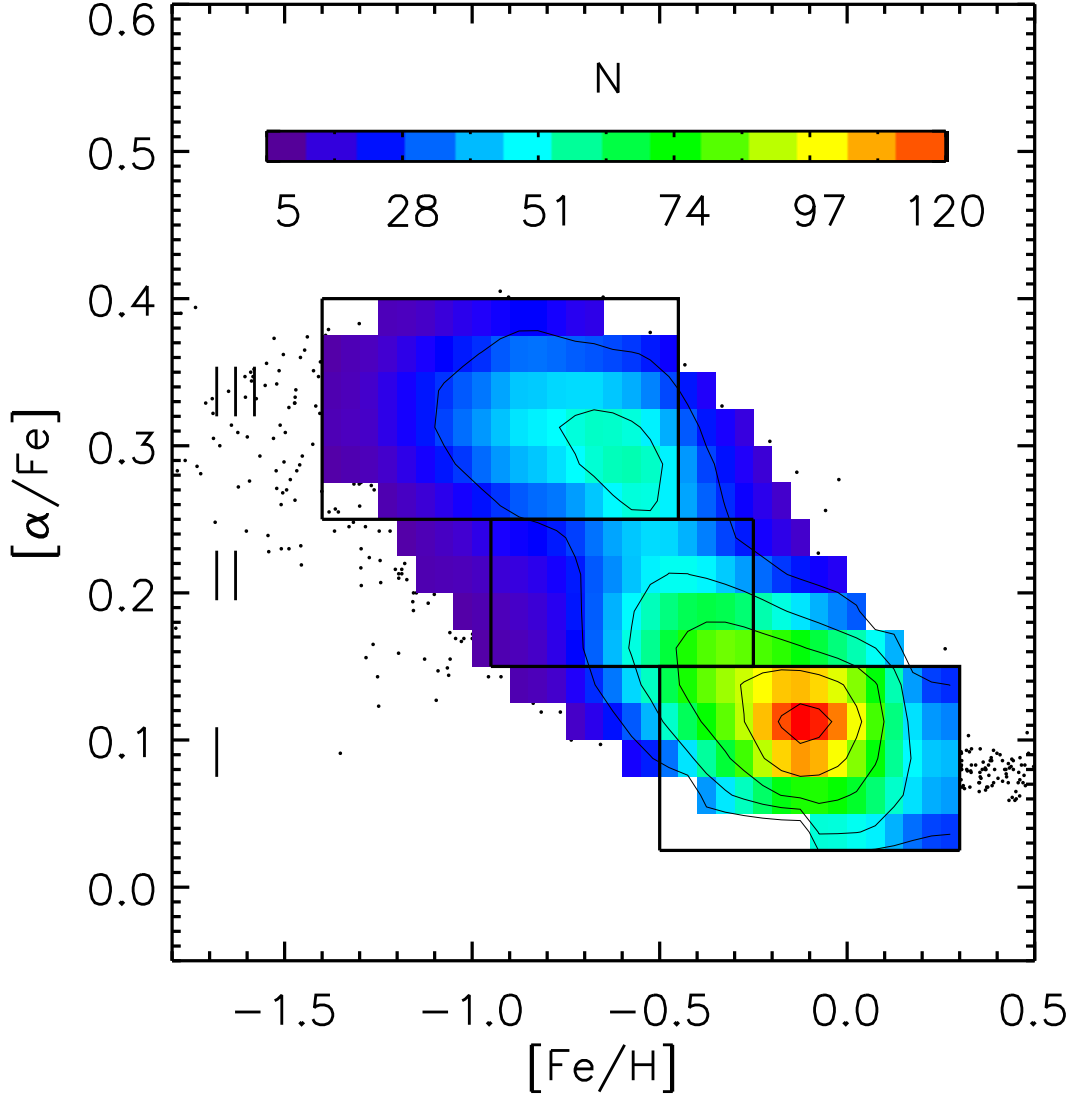


Fig. 1.— The unweighted number distribution of the 9157 K-dwarfs from SDSS/SEGUE used in our analysis, shown in the $[\alpha/\text{Fe}]$ - $[\text{Fe}/\text{H}]$ abundance space, with abundances taken from the SSPP (Lee et al. 2008a,b). As volume completeness corrections have not yet been taken into account, this distribution overemphasizes the metal-poor, α -enhanced stars (see Liu & van de Ven 2012; Bovy et al. 2012a). Black boxes indicate the three abundance-selected sub-populations. I: metal-rich ($[\text{Fe}/\text{H}] \in [-0.5, 0.3]$, $[\alpha/\text{Fe}] \in [0., 0.15]$); II: intermediate metallicity ($[\text{Fe}/\text{H}] \in [-1.0, -0.3]$, $[\alpha/\text{Fe}] \in [0.15, 0.25]$); III metal-poor ($[\text{Fe}/\text{H}] \in [-1.5, -0.5]$, $[\alpha/\text{Fe}] \in [0.25, 0.50]$).

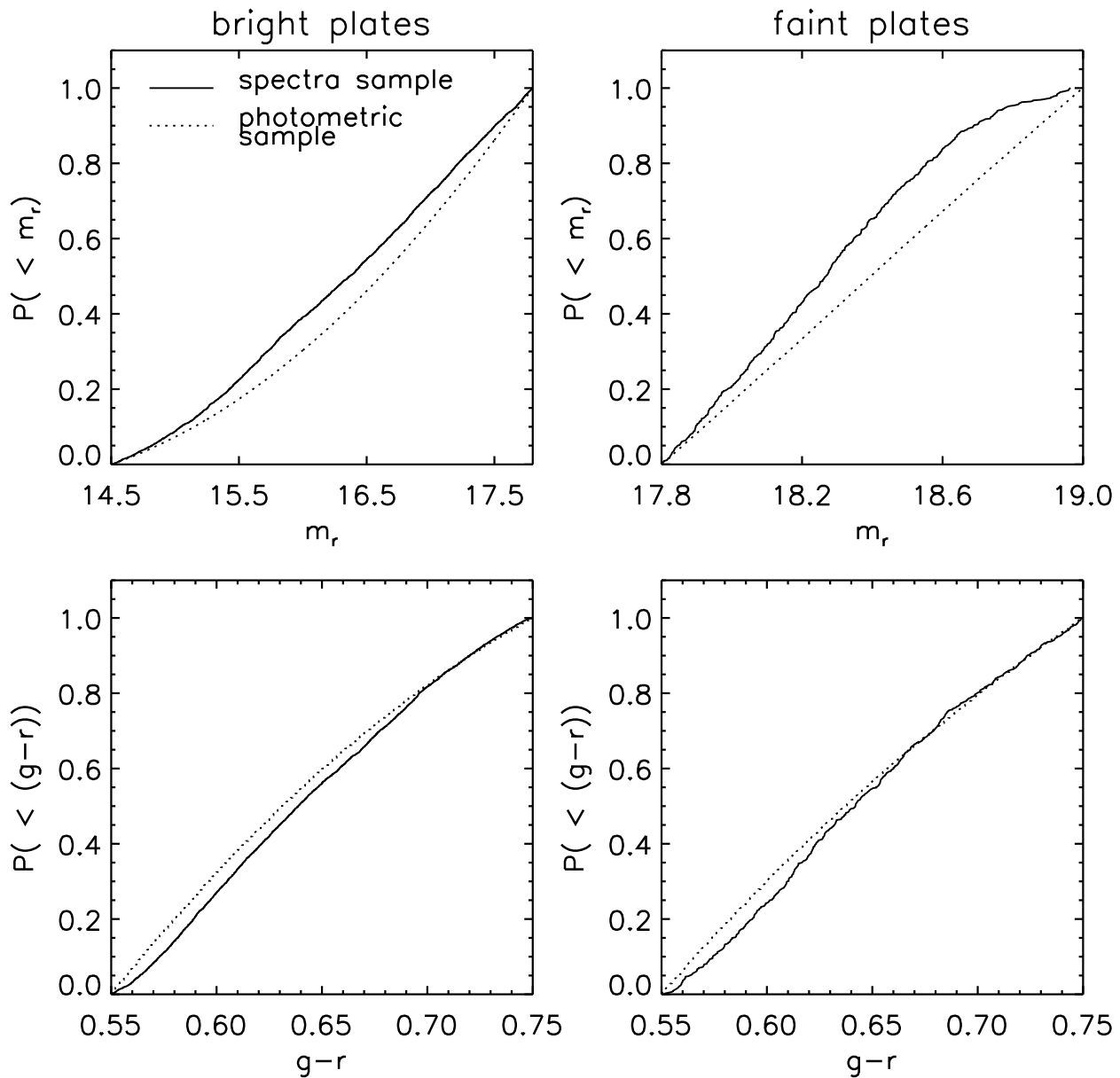


Fig. 2.— Spectroscopic success rate for K-dwarfs in SDSS/SEGUE, used to estimate the selection function (§ 3.1.2). The panels show the comparison of the distribution of the K-dwarfs that have good spectra from SEGUE (solid line) with the distribution of the presumably complete distribution of all photometrically detected point-source in the plate that satisfy the color-magnitude selection criteria.

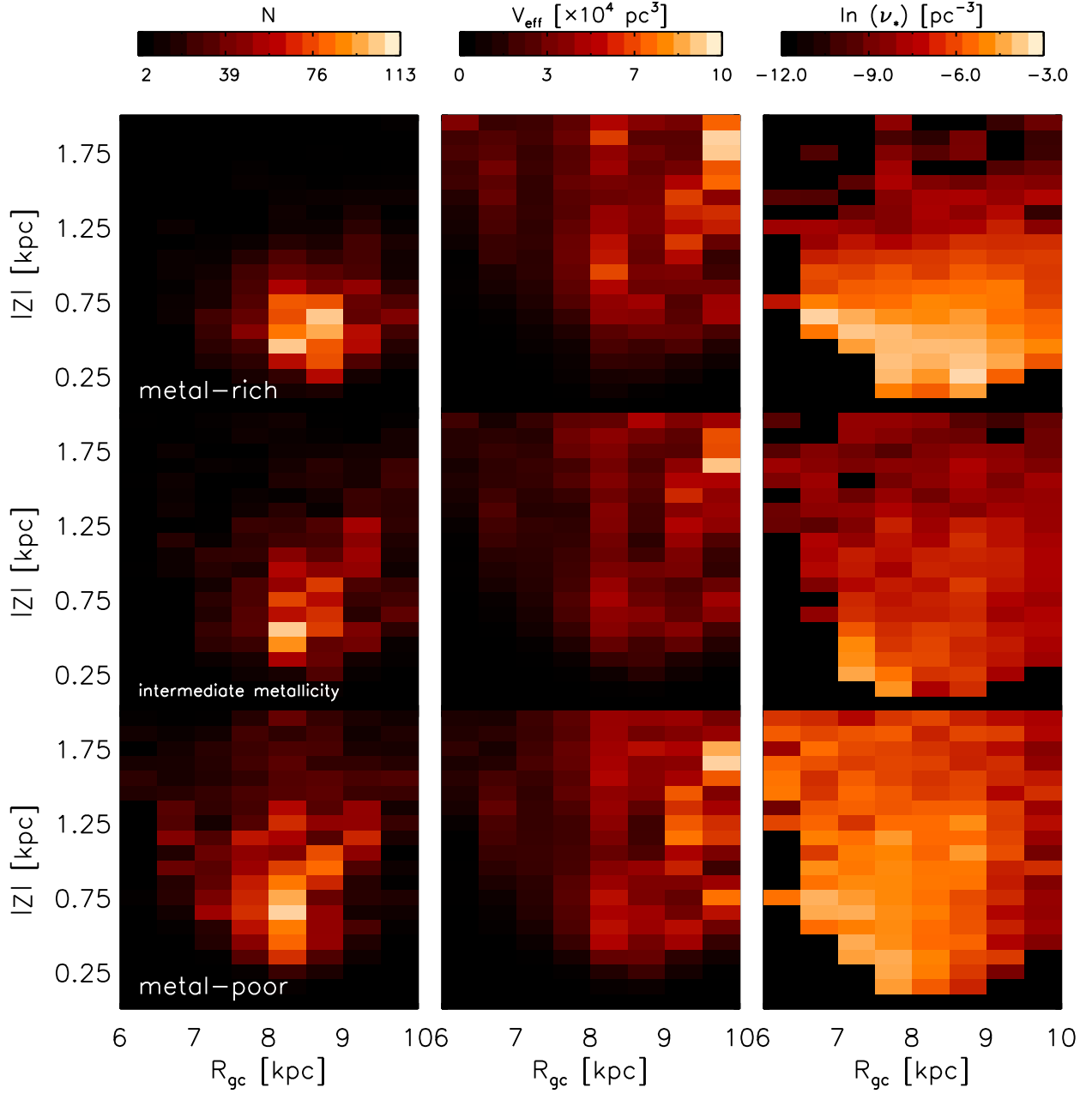


Fig. 3.— Derivation of the spatial tracer number density for each abundance-selected subsample. From top to bottom, plots show the metal-rich, intermediate metallicity, and metal-poor sub-populations, respectively. From left to right, the panels show the actually detected number of stars as a function of galactocentric distance and height above the plane, the effective survey volume, and the implied number density (see § 3.1).

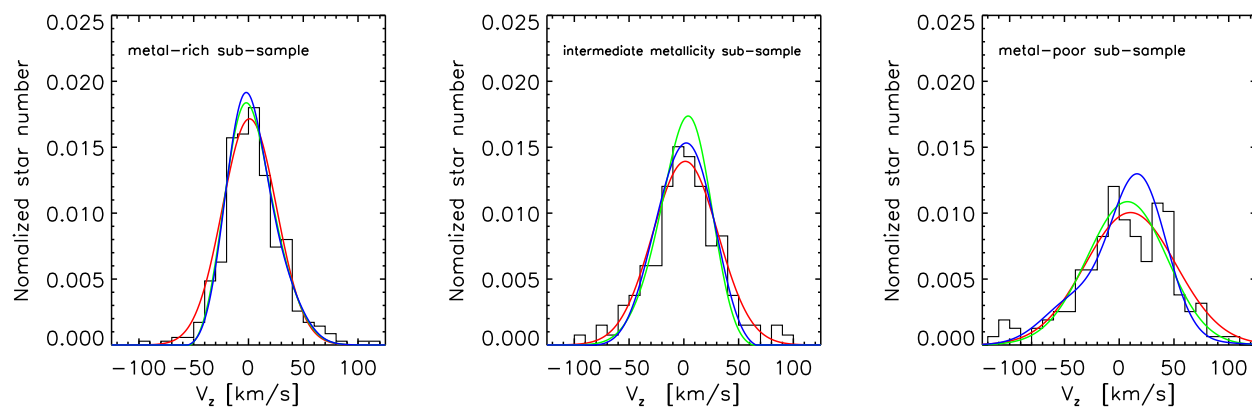


Fig. 4.— Example fits of the vertical velocity dispersion, shown for three abundance selected samples in the bin $600 \text{ pc} < |z| < 700 \text{ pc}$. For all panels, the histograms show the observed vertical velocity distributions, the red solid curves are Gaussian fits without considering observed errors, and the green and blue solid curves are three and four moments Gauss-Hermite accounting for the observational errors. Without taking the individual errors into account overestimates the vertical velocity dispersion by about 2 - 4 km/s.

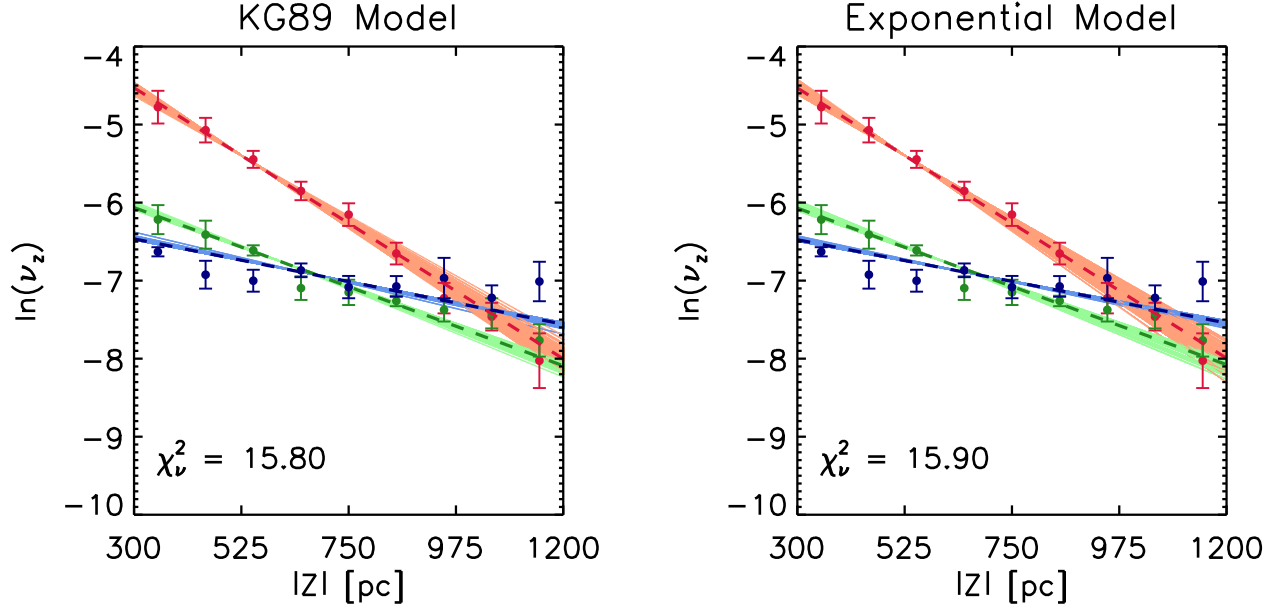


Fig. 5.— The derived vertical density profiles for the three abundance-selected sub-samples, with the model predictions from two of our parameterized models for the of K_z force profiles (the KG89 and exponential model, respectively; see Eq. 17 & 18). Filled circles are values estimated directly from the observations, dashed lines are model predicted values and shadows are the 68.3% errors in the recovered value of parameters. Red, green, blue symbols correspond metal-rich, intermediate metallicity, and metal-poor sub-population, respectively. χ^2_ν is calculated from the observed $\nu_{\star,\text{obs}}$ and modeled $\nu_{\star,\text{mod}}$ (Eq. 24).

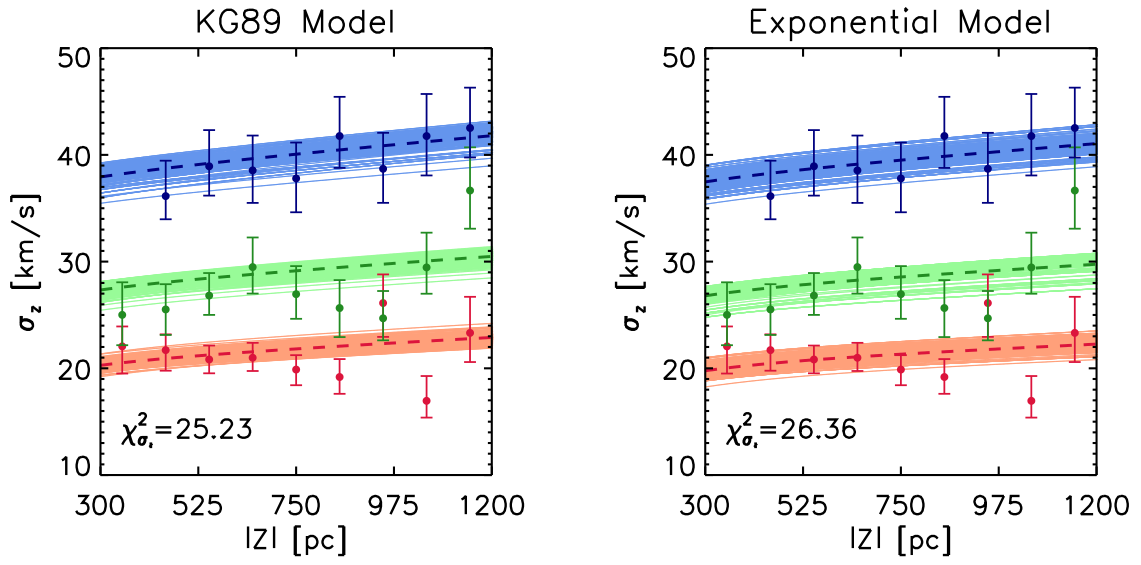


Fig. 6.— Analogous Figure to Fig. 5, but for vertical velocity dispersions.

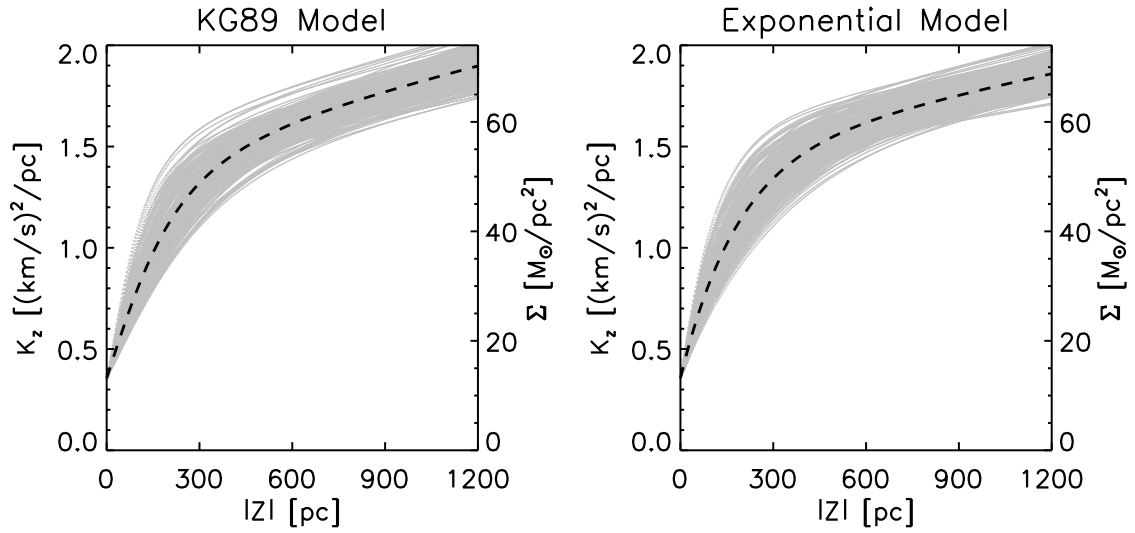


Fig. 7.— The vertical dependence of the K_z force of our two fiducial models, which include the stellar disk, a (thin) gaseous disk and a dark matter halo term. Left is the KG89 model (Eq. 17) and right is the exponential model (Eq. 18). In both panels, the dashed fat line shows $K_z(z)$ for the most likely parameters, and the band of grey points show a 1σ sampling of the PDF for K_z .

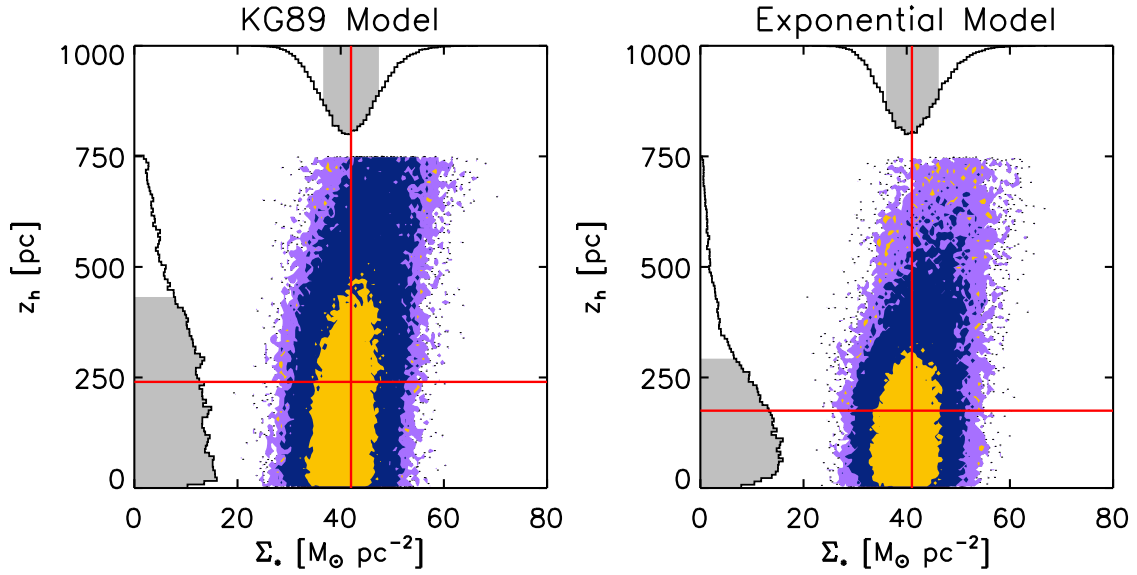


Fig. 8.— The PDF of model parameters Σ_* and z_h for the models in Eq. 17 & 18. On the left, the parameters for the KG89 model, on the right for the exponential model. Yellow, blue, and purple shades are 68%, 95%, and 99% confidence region, gray histograms are the marginalized PDFs for the individual parameters, and red lines represent the most likely value of each parameters.

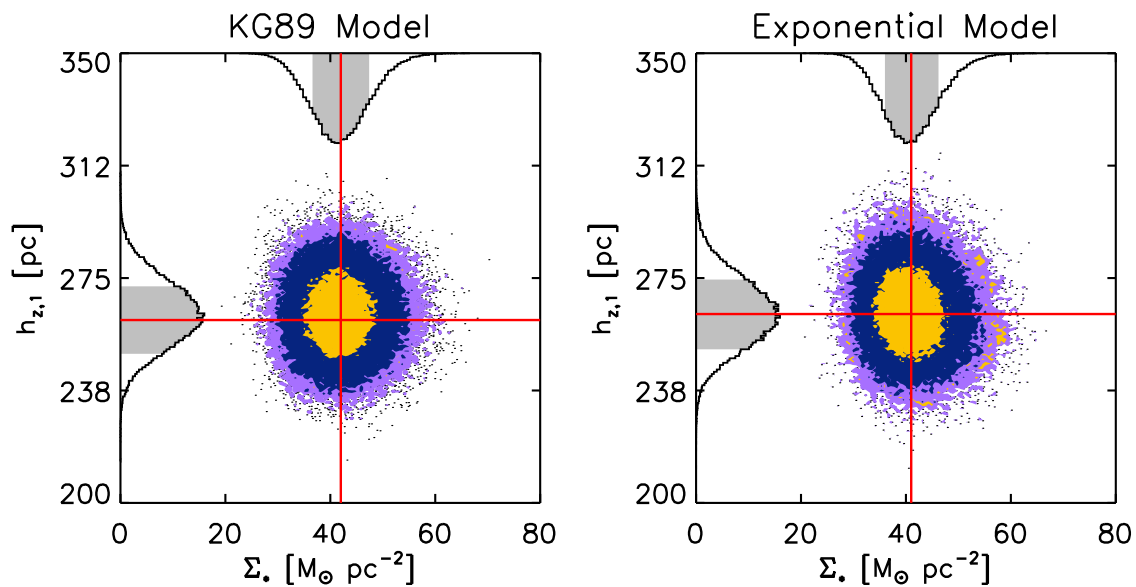


Fig. 9.— Analogous Figure to Fig. 8, but for the PDFs of Σ_* and the fitted scale height of the *tracer* population of stars, h_z , illustrated for the case of the metal-rich sub-population.

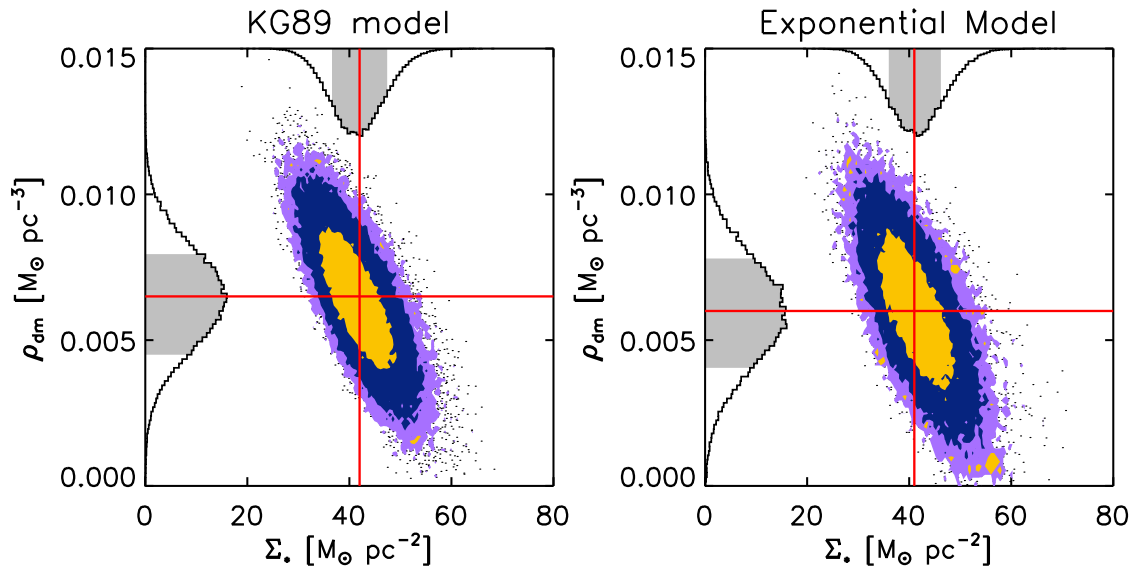


Fig. 10.— Analogous Figure to Fig. 8, but for the PDFs of ρ_{DM} and Σ_* .

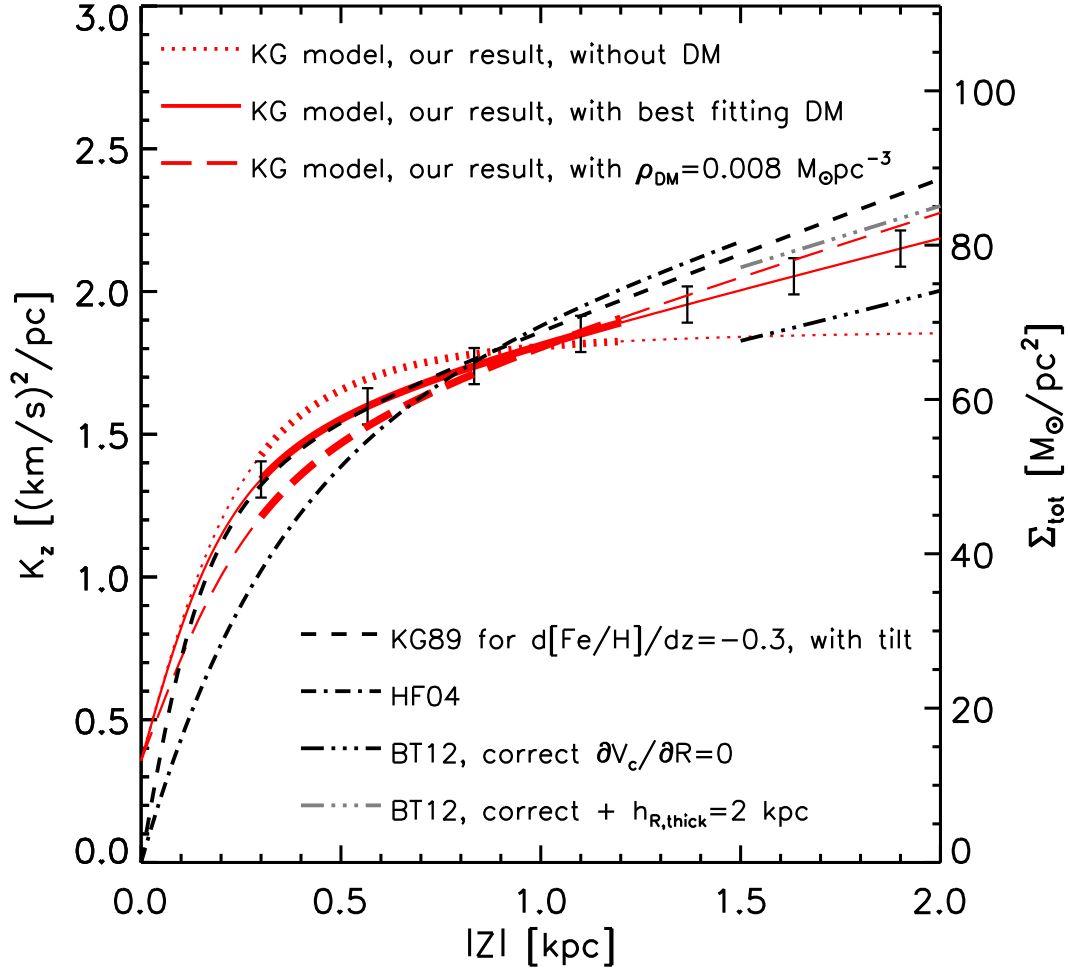


Fig. 11.— Comparison of the vertical force $K_z(z)$ and corresponding surface mass density $\Sigma_{\text{tot}, <|z|}$ implied by the best fits of the various model families to our data. The dotted, the dark solid, and the long dashed red lines represent three cases of our predictions based on KG89 model family: the one without DM (as a limiting case), the one with best fitting DM, and the one with $\rho_{\text{DM}} = 0.008 M_{\odot} \text{pc}^{-3}$ (from BT12), respectively. The 68% uncertainty intervals on the surface-mass density are shown at a few representative points. The $|z|$ range where the lines are drawn thicker represent the $|z|$ range of our sample stars. Dashed line is the same model but from the prediction of KG89.

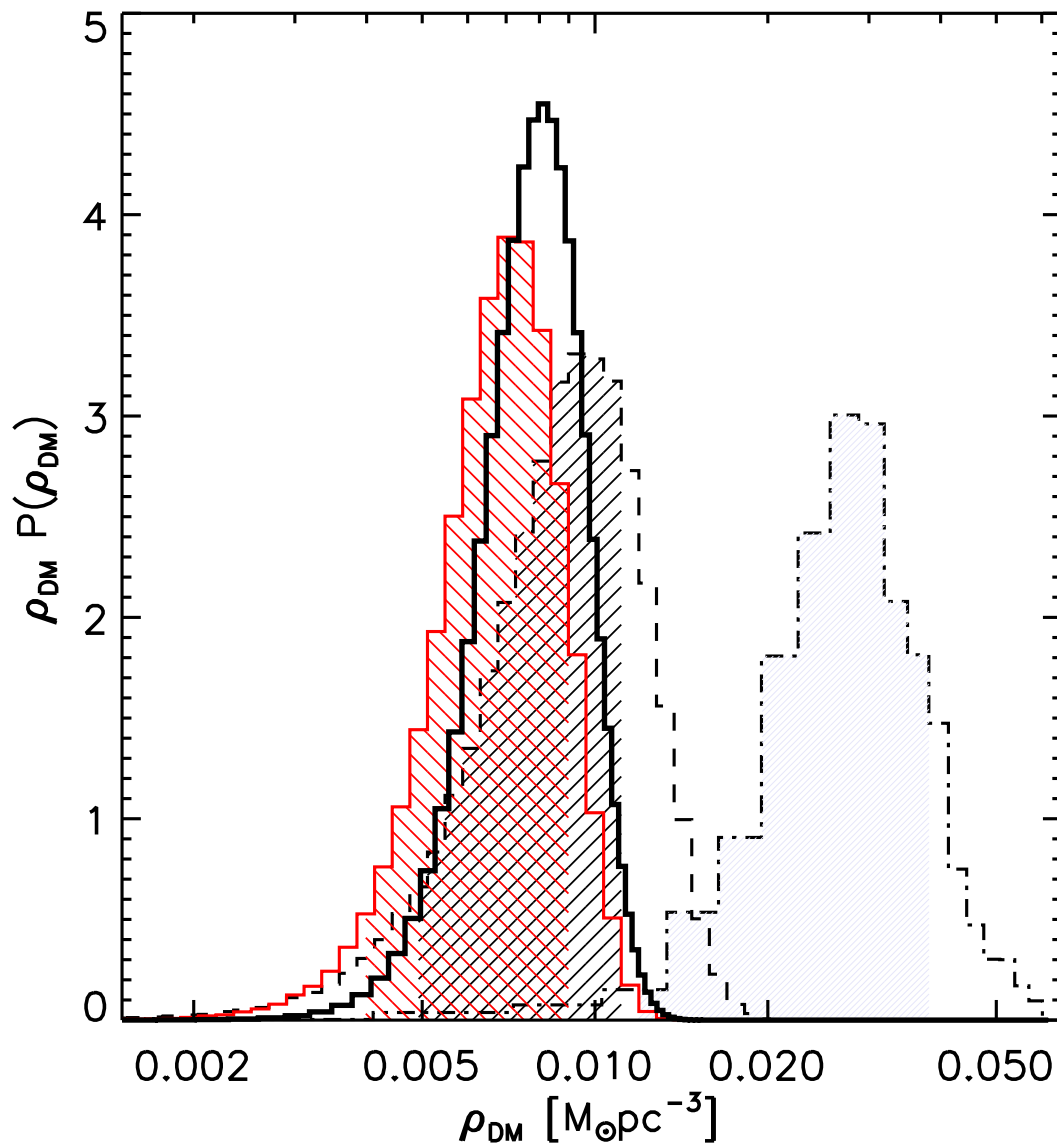


Fig. 12.— Comparison of normalized PDFs of ρ_{DM} derived by three independent works. The dashed dot line and gray shade represent the results of G12, dashed curve and shade are from the calculation of BT12, and red curve and shade are the results of our present work. Thicker black line means the joint PDF emerging from these three histogram.

Table 1: Fitting results of the two models, with $\Sigma_{\text{gas}} = 13 M_{\odot} \text{pc}^{-2}$ (Flynn et al. 2006)

	KG89 model (Eq. 17)	Exponential model (Eq. 18)
$\Sigma_{0,\text{star}} [M_{\odot} \text{pc}^{-2}]$	42 ± 6	41 ± 5
$\rho_{\text{DM}} [M_{\odot} \text{pc}^{-3}]$	0.0064 ± 0.0023	0.0060 ± 0.0020
$z_h [\text{pc}]$	245^{+188}_{-245}	200^{+100}_{-200}
$h_{z,1}^a [\text{pc}]$	259 ± 12	260 ± 15
$h_{z,2}^a [\text{pc}]$	450 ± 26	465 ± 33
$h_{z,3}^a [\text{pc}]$	852 ± 30	910 ± 71
$\sigma_{0,1}^a [\text{km/s}]$	15.4 ± 1.3	15.8 ± 1.3
$\sigma_{0,2}^a [\text{km/s}]$	23.0 ± 2.0	23.6 ± 2.0
$\sigma_{0,3}^a [\text{km/s}]$	34.2 ± 2.2	35.8 ± 2.2
$\chi_{\sigma_z}^2$	25.23	26.36
$\chi_{\nu_{\star}}^2$	15.80	14.54
χ_{tot}^2	41.03	40.90

^aNumber 1, 2, and 3 represent metal-rich, intermediate metallicity, and metal-poor sub-sample, respectively.